Article

"Green" Fabrication of High-Performance Transparent Conducting Electrodes by Blade Coating and Photonic Curing on PET for Perovskite Solar Cells

Justin C. Bonner [1,†], Robert T. Piper [1,†], Bishal Bhandari [2], Cody R. Allen [2], Cynthia T. Bowers [3,4], Melinda A. Ostendorf [3,4], Matthew Davis [5], Marisol Valdez [6], Mark Lee [2] and Julia W. P. Hsu [1,*]

1. Department of Materials Science and Engineering, University of Texas at Dallas, 800 W Campbell Road, RL-10, Richardson, TX 75080, USA
2. Department of Physics, University of Texas at Dallas, 800 W Campbell Road, Richardson, TX 75080, USA
3. Materials Characterization Facility at the Air Force Research Laboratory, 2941 Hobson Way, WPAFB, Dayton, OH 45433, USA
4. UES, Inc., A BlueHalo Company, 4401 Dayton-Xenia Rd., Dayton, OH 45432, USA
5. Energy Materials Corporation, 1999 Lake Ave B82 Ste B304, Rochester, NY 14650, USA
6. Department of Chemistry, University of Texas at Dallas, 800 W Campbell Road, Richardson, TX 75080, USA
* Correspondence: jwhsu@utdallas.edu
† These authors contributed equally to this work.

Abstract: This study presents an innovative material processing approach to fabricate transparent conducting electrodes (TCEs) on polyethylene terephthalate (PET) substrates using blade coating and photonic curing. The hybrid TCEs consist of a multiscale Ag network, combining silver metal bus lines and nanowires, overcoated by an indium zinc oxide layer, and then photonically cured. Blade coating ensures film uniformity and thickness control over large areas. Photonic curing, a non-thermal processing method with significantly lower carbon emissions, enhances the conductivity and transparency of the coated layers. Our hybrid TCEs achieve an average transmittance of $(81 \pm 0.4)\%$ referenced to air $((90 \pm 0.4)\%$ referenced to the PET substrate) in the visible range, an average sheet resistance of $(11 \pm 0.5)~\Omega~\text{sq}^{-1}$, and an average surface roughness of (4.3 ± 0.4) nm. We benchmark these values against commercial PET/TCE substrates. Mechanical durability tests demonstrate <3% change in resistance after 2000 bending cycles at a 1 in radius. The scalable potential of the hybrid TCE fabrication method is demonstrated by high uniformity and excellent properties in 7 in × 8 in large-area samples and by performing the photonic curing process at 11 m min^{-1}. Furthermore, halide perovskite solar cells fabricated on these hybrid TCEs achieve average and champion power conversion efficiencies of (10.5 ± 1.0) % and 12.2%, respectively, and significantly outperform devices made on commercial PET/TCEs. This work showcases our approach as a viable pathway for high-speed "green" manufacturing of high-performance TCEs on PET substrates for flexible optoelectronic devices.

Keywords: transparent conducting electrode; photonic curing; roll-to-roll; silver nanowires; blade-coating; "green" manufacturing

1. Introduction

Transparent conducting electrodes (TCEs) are critical components for many optoelectronic applications including transparent heaters, solar cells, light-emitting diodes, touch/display screens, Internet of Things (IoT), and wearable electronics [1,2]. TCEs fabricated on flexible substrates with non-planar form factor have applications in wearables and mounting on drones and tents [1]. Good TCEs require high optical transmittance (T), low electrical sheet resistance (R_{sh}) [3], and low surface roughness (σ_{rms}) [4]. Because materials with high electrical conductance ($1/R_{sh}$) typically have low optical transmission, optimizing both T and R_{sh} simultaneously is challenging [5]. The most common TCE is indium tin oxide (ITO). Highly crystalline ITO with superior properties, i.e., $T \sim 85\%$ (referenced to air) and $R_{sh} \sim 0$ Ω/sq, can be fabricated on rigid glass substrates. Vacuum deposition and high-temperature processing are needed to achieve these properties. When fabricating on flexible plastic substrates, desirable for their low cost and mechanical properties, large coefficients of thermal expansion (CTE) and low glass transition temperatures of plastics make high-temperature processing difficult or impossible. Consequently, ITO must be processed at lower temperatures, resulting in higher R_{sh} films. For example, one commercially available ITO film on a polyethylene terephthalate (PET) substrate has properties ($T \sim 80\%$ and $R_{sh} \sim 70$ Ω/sq) [6], inferior to typical rigid glass substrate counterparts ($T \sim 85\%$ and $R_{sh} \sim 10$ Ω/sq). To reduce R_{sh}, ITO films deposited on PET are thicker which leads to rougher films with less mechanical flexibility [7].

Currently, many alternatives to ITO are being investigated, including other transparent conducting oxides (TCOs), metal bus line (MBL) structures, metal nano-wire networks such as silver nanowires (AgNWs) or copper nanowires, carbon nanotubes, graphene oxide, and insulator/metal/insulator (IMI) structures, etc. [1,2,8,9]. MBLs can achieve extremely low R_{sh} values while maintaining high T, and can be fabricated with roll-to-roll (R2R) techniques such as gravure printing or flexography [10]. AgNWs offer excellent mechanical flexibility, optical and electrical properties, and solution processability [11]. However, there are several challenges with both MBLs and AgNWs. Highly transmissive MBLs typically have large gaps between metal lines, which reduces charge collection and efficiency for solar cells because charges do not diffuse over long distances. MBLs are also usually hundreds of nanometers tall to enable good electrical conduction, resulting in non-planar surfaces which can cause devices to be leaky or shorted [10]. Similarly, AgNWs produce rough films, leading to shunting in devices that require thin functional layers such as solar cells and light-emitting diodes [1].

All the above-mentioned TCE materials must be heated to high temperatures, typically by thermal annealing, for several minutes or even hours to achieve high T and low R_{sh}. For example, MBLs are typically made from metal colloidal inks which must be sintered at moderate temperatures (~100–150 °C) for tens of minutes to achieve good electrical conductance. AgNWs are commonly synthesized with a polyvinylpyrrolidone (PVP) coating to keep them suspended in solution [12], which causes high contact resistance at the joint between two AgNWs and must be removed through thermal or chemical treatment to form a highly conductive network. Metal oxides made from sol-gel precursors must also be thermally annealed to be fully converted to the desired compact oxide structure from the gel state. The conversion temperatures and times are typically high (200–500 °C) and long (>30 min), preventing the adaptation of solution-processed TCO films on plastic substrates. Furthermore, the long annealing time is incompatible with high-speed manufacturing, such as roll-to-roll (R2R), which can increase throughput and lower final product costs.

Additionally, 90% of industrial heat—the usage of heat in industries to transform materials into useful products—is produced by burning fossil fuels. In 2020, industrial heat accounts for nearly half of the emissions in industry, accounting for 9% of the entire U.S. emission footprint [13]. To circumvent the problems caused by thermal annealing and to reduce carbon emissions, here we employ photonic curing [14,15], also called intense pulsed light or flash lamp annealing, as a promising alternative. Photonic curing uses a xenon flash lamp that emits microsecond to millisecond pulses of broadband (200–1500 nm) light onto the sample. Light is selectively absorbed within the sample depending on the layers' optical properties, increasing temperature locally to facilitate material transformations such as crystallization, densification, or sintering. The short duration of light pulses translates to low energy delivered to the samples, avoiding damage to low thermal-budget PET substrates; furthermore, the short pulses make photonic curing compatible with high-throughput R2R fabrication. The electricity use of a photonic curing tool is efficient because the energy is delivered only to the specific thin films without heating the environment. Thus, photonic curing is a "green" material processing method that is both high-speed and compatible with plastic substrates. Photonic curing has been applied to a plethora of materials, including AgNWs [16–20], metal inks [21–23], halide perovskite [24–28], and metal oxides [27, 29–33].

In this work, we fabricate hybrid TCEs at room temperature by blade-coating material layers on PET substrates containing flexographically printed MBLs and process them with photonic curing. A techno-economic report has shown that combining solution deposition and photonic curing enables R2R manufacturing with a lower-

cost final product by taking advantage of inexpensive capital expenditure and the economy of scale [34]. To solve the challenges created by MBLs or AgNWs alone, we create a hybrid TCE structure consisting of a multiscale Ag network of MBLs and AgNWs overcoated by a sol-gel indium zinc oxide (IZO) film. The entire hybrid TCE structure is processed with photonic curing, instead of high-temperature thermal annealing. In this hybrid TCE structure of multiscale Ag network and IZO, the Ag MBLs act as highly conductive "highways" to achieve overall low R_{sh}, the AgNWs act as slightly less conductive "streets" to increase charge collection in the gaps between the Ag MBLs, and the IZO acts as both charge collection material in the gaps between the AgNWs and planarization to decrease the σ_{rms} of the hybrid film. IZO was chosen as the planarization layer because it can be made by combustion sol-gel chemistry that requires less energy and IZO is less crystalline than ITO, thus better mechanical durability. These hybrid TCEs are targeted for halide perovskite solar cells (PSCs), with the desired properties of average transmittance from 400 to 700 nm wavelengths (T_{avg}) ³ 80% (referenced to air), $R_{sh} < 15\ \Omega\ sq^{-1}$, and $\sigma_{rms} < 5$ nm. While several research groups have fabricated MBL and/or AgNW TCEs with an overcoated layer to smooth the MBL and/or AgNW surface using thermal annealing [11, 35–43], none demonstrated that their process was compatible with large-area and photonic curing, i.e., high-throughput R2R manufacturing.

First, we fabricated small-area (1 in × 3 in) samples and measured their T_{avg}, R_{sh}, and σ_{rms}, which are benchmarked against commercially available PET/TCEs. Bending tests were also performed to evaluate the mechanical durability and the suitability of conveying these TCEs on an R2R machine for optoelectronic device fabrication. Next, the blade-coating was scaled up to fabricate 7 in × 8 in hybrid TCEs, and the photonic curing process speed was increased to 11 m min⁻¹. Finally, to demonstrate the performance of these hybrid TCEs, we fabricated PSCs on top of them to evaluate the quality of hybrid TCEs made under different processing conditions. By combining blade coating and photonic curing, this work showcases a viable pathway for ambient environment fabrication of high-quality TCEs on PET substrates at high speeds, paving the way for future development of sustainable R2R manufacturing of PSCs.

2. Methods

2.1. Materials

Poly(3,4-ethylenedioxythiophene) polystyrene sulfonate (PEDOT:PSS, Clevios 4083) solution was purchased from Heraeus Deutschland (Hanau, Germany). (2-(3,6-Dimethoxy-9H-carbazol-9-yl)ethyl)phosphonic acid (MeO-2PACz) and lead iodide (PbI₂) were purchased from TCI America (Montgomeryville, OR, USA). Methylammonium iodide (MAI) was purchased from GreatCell Solar (Queanbeyan East, Australia). Phenyl-C₆₁-butyric acid methyl ester (PCBM) was purchased from Lumtec. Silver nanowires were purchased from Cheap Tubes Inc (Grafton, VT, USA). and Sigma-Aldrich (St. Louis, MO, USA). All other chemicals were purchased from Sigma-Aldrich or Fisher Scientific (Pittsburgh, PA, USA). All chemicals were used as received, unless otherwise stated. Specific information on PET substrates with MBLs is given in the supplementary materials.

2.2. Indium Zinc Oxide Solution Preparation

The indium zinc oxide (IZO) solution was made by dissolving 0.4 M indium nitrate hydrate and 0.4 M zinc nitrate hexahydrate in two separate vials of 2-methoxyethanol (2-MOE) [44]. The solutions were allowed to dissolve for a minimum of 4 h. The day before using the solution, 0.7 M of acetylacetone and 0.6 M of ammonium hydroxide were added to both the indium nitrate and zinc nitrate solutions, separately, and mixed for ~12–15 h. On the day of coating, the indium nitrate and zinc nitrate solutions were mixed in a 7:3 In:Zn atomic ratio and diluted with 2-MOE to have a total metal salts (In + Zn) concentration of 0.2 M. This IZO precursor was then mixed for at least 1 hr. The solution was filtered with a 0.2 μm polytetrafluoroethylene filter just before blade-coating.

2.3. Blade Coating

All hybrid transparent conducting electrode fabrication processes were done in ambient conditions; the temperature (21–25 °C) and relative humidity (30–65%) were not controlled. For small-area coatings, ~100 μm thick PET/MBL substrates were cut into 1 in (cross-web direction) × 3 in (down-web direction) rectangles. The substrates were ultrasonically cleaned in soapy water (Alconox) for 10 min followed by rinsing in deionized (DI) water, acetone, IPA, and DI water, and then blown dry with nitrogen immediately before coating. The Ag metal lines are oriented perpendicular to the down-web direction. A layer of AgNWs was first deposited onto the PET/MBL substrate via blade-coating (MTI Corporation MSK-AFA-III) using a blade-gap (measured from the bottom of the blade to the top of the substrate) of 510 μm and a dispensed volume of 50 μL. After blade-coating,

the sample was placed on a 90 °C hot plate for 2 min to dry off the solvent. Then, a layer of IZO was blade-coated on top of the AgNW layer using a blade gap of 410 μm and a dispensed volume of 25 μL. Both layers were coated at a speed of 1.5 m min^{-1}. The IZO film was allowed to relax for 90 s before transferring the sample to a 90 °C hot plate for 2 min to dry. The sample was then transferred directly from the hot plate to the photonic curing tool and processed in air. After photonic curing, the sample was rinsed with DI water to remove any excess unconverted precursor materials, followed by blowing dry with nitrogen. Finally, a second layer of IZO was then blade-coated following the same steps listed above for the first IZO layer. Photonic curing was completed then the sample was rinsed and blown dry again. For large-area coatings ~175 μm thick PET/MBL substrates were cut to 7 in (cross-web direction) × 8 in (down-web direction) rectangles. A nitrogen gun was used to remove particles from the surface, with no other cleaning or preparation steps. A Zehntner ZAA 2300 blade-coater was used with an 8 in ZUA 2000 blade-applicator. An air knife on the blade-applicator was used for AgNW coatings, but not for IZO coatings. The blade gaps used for AgNW and IZO coatings were 350 μm and 275 μm, respectively. The dispense volumes for the AgNW and IZO coatings were 230 μL and 170 μL, respectively. Both layers were coated at a blade speed of 1.8 m min^{-1}. All other steps in the coating process are the same as explained for small-area coatings.

2.4. Photonic Curing

Photonic curing for small-area samples was completed using a PulseForge Invent equipped with three 950 V lamp drivers (NovaCentrix, Austin, TX, USA), a 1.5 kW power supply, and a 20 mm diameter × 150 mm long xenon flash lamp that provides a uniform illumination area of 75 mm × 150 mm. The samples were photonically cured after transferring directly from the hot plate to the photonic curing tool. The samples were held down onto the aluminum stage, roughly 5 mm from the xenon flash lamp, using two magnetic metal slats. All samples were photonically cured using either 9-pulse or 1-pulse conditions. The 9-pulse condition uses 300 V lamp voltage, 25 ms pulse length, 24 micro-pulses, 45% duty cycle, 9 pulses, 0.15 Hz pulse repetition rate, and ~3.5 J cm^{-2} fluence. The 1-pulse condition uses 315 V lamp voltage, 10 ms pulse length, 24 micro-pulses, 65% duty cycle, and ~3.6 J cm^{-2}. The lamp voltage is adjusted depending on the tool and age of the lamp such that the intended radiant energy is measured. To process the large-area samples, a PulseForge Invent is mounted on a R2R system; this photonic curing tool is equipped with three 950 V lamp drivers, two 15 kW power supplies, and a 20 mm diameter × 300 mm long xenon flash lamp that provides a uniform illumination area of 75 mm × 300 mm. Coated hybrid TCE samples are taped down to the PET web and conveyed under the lamp at a constant web speed. The photonic curing parameters are adjusted to closely match the 9-pulse condition established for small-area samples at 3.5 J cm^{-2} fluence, by using 410 V lamp voltage, 25 ms pulse length, 24 micro-pulses, 45% duty cycle, 9 pulses, 1.2 overlap factor, and 0.25 m min^{-1} web speed. For the stitching experiments, a PulseForge Invent with three 950 V lamp drivers, 15 kW power supply, and 20 mm diameter × 150 mm long xenon flash lamp is used. To match the 1-pulse condition at 3.6 J cm^{-2} fluence, the lamp voltage is adjusted to 320 V, with 10 ms pulse length, 24 micro-pulses, 65% duty cycle, 1.2 overlap factor, and 11 m min^{-1} web speed.

2.5. Materials Characterization

Scanning electron microscope (SEM) images were taken on a Zeiss Sigma 500 VP SEM with an acceleration voltage of 500–1000 V (Zeiss, White Plains, NY, USA). Atomic force microscopy (AFM) images were taken using an Asylum Research MFP-3D system (Oxford Instruments, Concord, MA, USA) in tapping mode to determine σ_{rms}. Average σ_{rms} was calculated from at least three 10 μm × 10 μm areas. UV-vis transmission was measured with an Ocean Optics 4000 USB spectrometer. Ultraviolet-visible-near infrared transmission was measured with an Agilent Technologies Cary 5000 Spectrometer. The average transmittance T_{avg} was calculated between 400 and 700 nm and the $T_{avg,NIR}$ was calculated between 400 and 1200 nm. Sheet resistance (R_{sh}) was measured with a Bridge Technology SRM-232-100 four-point probe with ~1 mm probe spacings. For small-area samples, R_{sh} was measured four times in the center of the down-web direction in 1 in × 3 in samples. The sample was rotated 45° between each measurement and the reported value is the average of these 4 measurements. For large-area samples, both T_{avg} and R_{sh} were measured in nine locations across the 7 in × 8 in sample.

X-ray photoelectron spectroscopy (XPS) was performed using an Ulvac-PHI VersaProbe2 (Ulvac-PHI, Chigasaki, Kanagawa, Japan) with a monochromatic Al Kα source (1486.8 eV, 50 W, 15 kV) with a 200 μm beam diameter and a 45° angle to the sample. The O 1s, Ag 3d, In 3d, and Zn 2p spectra were averaged over 20 scans with an energy step of 0.1 eV for 20 ms per step and a pass energy of 23.5 eV. The N 1s spectrum was averaged over 100 scans with an energy step of 0.2 eV for 20 ms per step and a pass energy of 187.85 eV. XPS fitting was done using CasaXPS software (Casa Software Ltd., Wilmslow, England, UK). All fits used 70:30 mixed Gaussian:Lorentzian functions. A 10 μA neutralizer was used at a bias voltage of 3 V.

Transmission electron microscopy (TEM) lamella of a hybrid TCE were made using an FEI NOVA NanoLab 600 Dual Beam SEM/FIB equipped with a Ga liquid metal ion source (Nanolab Inc., Waltham, MA, USA). The focused ion beam (FIB) was operated at 16 kV. Prior to FIB milling, carbon was evaporated onto the surface to increase conductivity, and a permanent ink marker was used to apply a protective cap. Each lamella was attached to a Mo grid at two points with an ion beam deposited Pt and subsequently thinned using smaller and smaller currents as the lamella thickness decreased. TEM observations were made using a ThermoFisher Scientific Talos F200X operated at an accelerating voltage of 200 kV. Samples were imaged both in TEM and scanning TEM (STEM) modes. STEM mode employs a high-angle annular dark field (HAADF) detector that enables X-ray energy dispersive spectroscopy (XEDS, ThermoFisher Scientific., Waltham, MA, USA) to be carried out using a Quantax microanalysis system controlled by Bruker Espirit software. Samples were mapped with the HyperMap function which recorded a full spectrum at every point of the map. Microanalysis was carried out without using standards for a semi-quantitative analysis.

Bending test of the hybrid TCE was performed using an Instron E10000 (Instron, Norwood, MA, USA) in tensile test mode. For thickness measurements, materials on hybrid TCEs were removed using a Spectra-Physics Explorer One HP 355-4 nanosecond solid state 355 nm laser, or the hybrid TCE was purposely cracked and areas were removed using scotch tape. The laser scribing was done at 500 mm/s and 20 kHz and fluence was varied from 8 to 56 J to find the optimal scribed depth. To measure hybrid TCE *d*, a Keyence optical profilometer (VK-X3100 measurement head with VK-D3 stage, Keyence, Osaka, Japan) was used under the laser (404 nm wavelength) confocal mode. The measurement head is equipped with a 50× objective lens with 12 nm *z* resolution and 40 nm *x-y* resolution.

2.6. Perovskite Solar Cell Fabrication and Testing

PSCs were fabricated on 1 in × 1 in hybrid TCEs, which were used as made without any additional cleaning or UVO treatment. The flexible substrates were then mounted onto a thin, rigid piece of glass (0.5 mm) for device fabrication and handling. The *p-i-n* device architecture was used, composed of the following layers from bottom to top: hybrid TCE/neutral PEDOT:PSS/regular PEDOT:PSS/MeO-2PACz /methylammonium lead iodide (MAPbI$_3$)/PCBM/bathocuproine (BCP)/Al/Ag. The regular PEDOT:PSS solution was made by mixing as-received PEDOT:PSS (Clevios 4083) and IPA in a 7:3 ratio on a 50 °C hot plate for 30 min. For neutral PEDOT:PSS, ammonium hydroxide was added in a 5:1 ratio (PEDOT:PSS:ammonium hydroxide) and mixed for an additional 15 min. Adding ammonium hydroxide increased the pH of the solution from 1.7 to 7. MeO-2PACz (2 mg mL^{-1} unless specified) was dissolved in anhydrous ethanol for 1 h without heat inside a nitrogen glovebox. For PSCs made with the neutral/regular PEDOT:PSS bilayer and MeO-2PACz, the neutral PEDOT:PSS solution was first spin-coated at 4000 RPM for 30 s and thermally annealed at 120 °C for 10 min on top of the PET/TCE substrate following the same procedures above for the regular PEDOT:PSS to form a bilayer. Then, MeO-2PACz was spin-coated at 3000 rpm for 30 s on top of the regular PEDOT:PSS in the fume hood and then immediately transferred into a nitrogen glovebox for annealing at 100 °C for 10 min. After the deposition of the MeO-2PACz layer, the sample was ready for MAPbI$_3$ deposition. The anti-solvent-free MAPbI$_3$ precursor formulation was modified from a previous study [45]. The solution was prepared inside a nitrogen glovebox by dissolving an equal molar ratio of PbI$_2$ and MAI in 2-MOE (0.8 M) and adding N- Methylpyrrolidone (NMP) (40 mol% of MAPbI$_3$). The MAPbI$_3$ precursor solution was mixed for at least 3 h before use. The samples and MAPbI$_3$ precursor solution were transferred into a nitrogen purge box with relative humidity between 1% and 3%. The MAPbI$_3$ solution was spin-coated at 5000 RPM for 20 s and then thermally annealed on a hot plate inside the purge box at 100 °C for 10 min. Next, PCBM (20 mg mL^{-1} in chlorobenzene) was spin-coated at 1200 RPM for 60 s, followed by spin-coating BCP (0.5 mg mL^{-1} in ethanol) at 4000 RPM for 30 s. Finally, 100 nm of Al and 50 nm of Ag were thermally evaporated in a nitrogen glovebox as top contacts. Six 0.11 cm^2 diodes were created on each 1 in × 1 in substrate. The final devices were stored in the nitrogen glovebox, in the dark, overnight before device testing. The current density-voltage (*J-V*) measurements were performed under an AM 1.5G 100 mW cm^{-2} AAA solar simulator (Abet) in a nitrogen glovebox using a Keithly 2635A source meter. The illumination aperture size was 0.049 cm^2. The applied voltage was ramped from −0.2 V to 1.2 V for the forward scan and from 1.2 V to −0.2 V for the reverse scan, at a ramp rate of 70 mV s^{-1}.

3. Results and Discussion

3.1. Fabrication of 1 in × 3 in Hybrid TCE

A workflow of the hybrid TCE fabrication process is given in Figure 1. SEM micrographs (above the schematics in Figure 1) at each processing step show good film uniformity and spatial distribution of AgNWs across the film (Figure 1b). A high-magnification SEM micrograph of the AgNWs is given in Supplementary Figure S1. The IZO precursor film appears to have some phase separation, visible by the large dark spots on the film, Figure 1c. However, after photonic curing and rinsing, Figure 1d, the film surface appears uniform and the AgNWs and Ag MBLs are fully covered by the IZO layer, further evidenced below. The IZO blade-coating and photonic curing processes, Figure 1c,d, may be repeated to deposit additional layers of IZO. Transmittance spectra after each step in Figure 1 are given in Supplementary Figure S2.

The photonic curing parameters are modified from our previous spin-coated PET/AgNW/IZO work, which did not include Ag MBLs [17]. In that work, the photonic curing condition used 350 V lamp voltage that produced 5.1 J cm^{-2} fluence. However, this fluence must be reduced because the Ag MBLs absorb a significant amount of the radiant energy, which results in overheating and ablation of the MBLs or melting of the underlying PET substrate. An example is shown in Supplementary Figure S3. Thus, the lamp voltage was lowered to 300 V, with the other photonic curing parameters fixed (25 ms pulse envelope, 24 micro-pulses, 45% duty cycle, 9 pulses, 0.15 Hz pulse repetition rate), resulting in 3.5 J cm^{-2} fluence without damaging the MBLs. These processing conditions, referred to as the 9-pulse condition, lead to a total photonic processing time of 53 s.
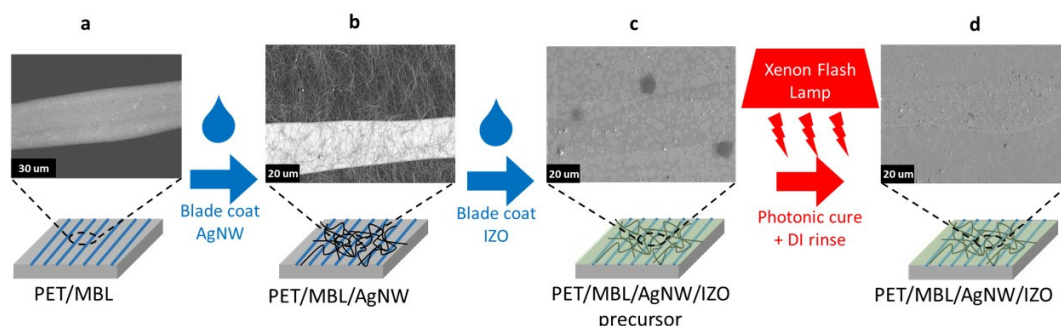

Figure 1. Process workflow for blade-coating and photonic curing AgNWs (black) and IZO (green) on top of PET/MBL (PET in gray and Ag MBL in blue) substrates: (**a**) The PET/MBL substrate consists of a 100 μm thick PET with flexographically printed Ag MBLs (~120 nm tall and ~30 μm wide). (**b**) A layer of AgNWs is blade-coated on top of the PET/MBL substrate. (**c**) A layer of IZO is blade-coated on top of the AgNW layer and dried on a hot plate at 90 °C for 2 min. (**d**) After drying, the sample is immediately photonic cured followed by rinsing with deionized water to remove any excess unconverted precursor materials. SEM micrographs are shown above each processing step.

3.2. Hybrid TCE Properties

Figure 2a shows a picture of the final hybrid TCE (PET/MBL/AgNW/IZO) fabricated via blade-coating and photonic curing on top of a University of Texas at Dallas (UTD) logo. The TCE edges are denoted by the two red dashed lines. Figure 2b shows a 10 μm × 10 μm atomic force microscopy (AFM) image of the hybrid TCE, indicating a smooth morphology with high points near AgNW junctions. The σ_{rms} of the AgNW layer alone on PET/MBL is (14.4 ± 1.0) nm, which improves after a single coat of IZO to (9.6 ± 0.9) nm but is still too rough for efficient PSC device fabrication (Supplementary Figure S4). High surface roughness causes device shunting; therefore, two layers of IZO are required to effectively planarize the hybrid TCE film. Additional IZO layers can further planarize the surface; however, the CTE mismatch between PET and metal oxide causes cracking of the IZO layers when the IZO is too thick during mild heating steps (100–120 °C) in device fabrication. The low σ_{rms} values of the final hybrid TCE, measured at several locations across the TCE, indicate that the IZO layer is planarizing the rough AgNW surface. Figure 2c shows an SEM image of the edge of the IZO coating to demonstrate that the IZO is overcoating and planarizing both AgNWs and MBLs. On the left side of Figure 2c, i.e., with the IZO layer, a faint impression of the Ag MBL can be discerned. Supplementary Figure 1b shows a higher magnification image of AgNWs overcoating the Ag MBLs, ensuring good electrical contact between the two. The center of hybrid TCE is highly uniform with AgNWs fully covered by IZO, as seen in Figure 2d. The final hybrid TCE is highly conductive, optically transparent, and smooth with $T_{avg} = (81 ± 0.4)\%$ referenced to air ((90 ± 0.4)% referenced to PET), $R_{sh} = (11 ± 0.5)$ Ω sq^{-1}, and $\sigma_{rms} = (4.3 ± 0.4)$ nm. For reference, we also blade-coated and photonic-cured AgNWs and IZO on bare PET substrates without Ag MBLs using the same processing procedures. Without MBLs, the TCEs exhibit $T_{avg} = (83 ± 0.3)\%$ referenced to air and $R_{sh} = (34 ± 7)$ Ω sq^{-1}. Our

previous work using spin coating for deposition was done on PET without MBLs and achieved $T_{avg} = (77 \pm 2.2)$ % and $R_{sh} = (15 \pm 3.7)$ Ω sq^{-1} [17]. Therefore, Ag MBLs are needed to produce a hybrid TCE with a target T_{avg} of >80% referenced to air and R_{sh} of <15 Ω sq^{-1}.

To evaluate the metal oxide conversion and chemical composition of the IZO layer in the hybrid TCE film, we performed XPS. The measurement and fitting details are given in the experimental section. Figure 3a,b show the O 1s and N 1s spectra, respectively, comparing the dried precursor film in black (Figure 1c) and the final hybrid TCE film in red (Figure 1d). The XPS spectra for Ag 3d, In 3d, and Zn 2p are given in Supplementary Figure S5. The two peaks in the O 1s spectra are from metal hydroxide species at ~532 eV (green-shaded region) and metal oxide species at ~530 eV (magenta-shaded region) [46,47]. The metal oxide O 1s peak is absent in the precursor film but present after the photonic curing process, indicating that metal oxide is formed by photonic curing. We also identified two peaks in the N 1s spectra, one for nitrate species at ~407 eV and one for various nitrogen species including amines and nitric oxide at ~400 eV [48]. The ~407 eV peak arises from the metal nitrate salts used as the IZO precursor materials. After photonic curing, the nitrate peak reduces to almost background noise, indicating that the metal nitrates have been decomposed by the light to initiate the sol-gel conversion to metal oxides. To determine the chemical composition, the atomic ratio of In:Zn was calculated to be 81:19 for dried precursor films and 96:4 for the final hybrid TCE film while the IZO precursor solution has an atomic ratio of 70:30. This indicates that more indium remains in the film after processing, in agreement with the lower decomposition temperature of indium nitrate (~212 °C) compared to zinc nitrate (~326 °C) (Supplementary Figure S6). Thus, more indium nitrate is converted to oxide during photonic curing than zinc nitrate, leading to a higher atomic percentage of indium in the final IZO film.
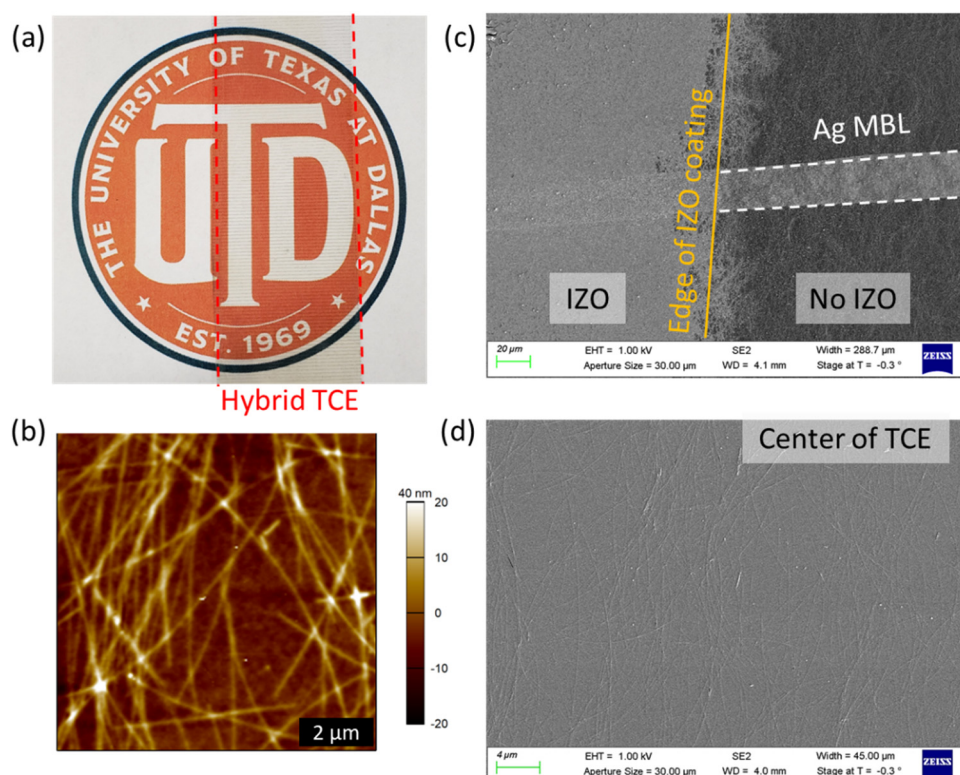

Figure 2. Hybrid TCE characterization at macro and micro scales: (**a**) Optical image, (**b**) AFM micrograph (10 µm × 10 µm), and SEM micrographs (**c**) at the edge of the IZO coating and (**d**) at the center of the hybrid TCE.
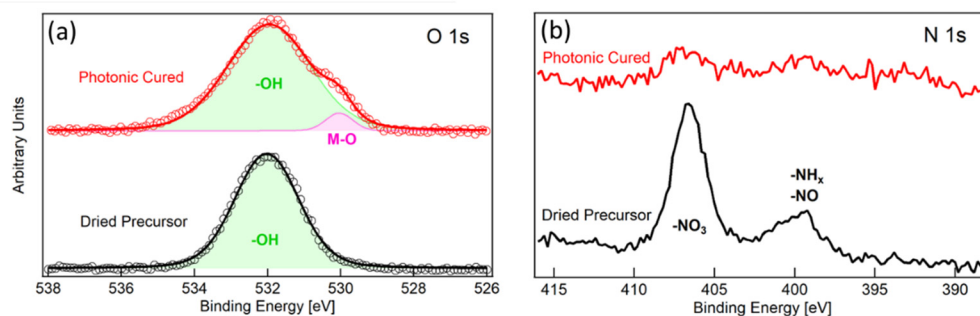
Figure 3. XPS spectra for hybrid TCE before and after photonic curing: (**a**) O 1s and (**b**) N 1s comparing dried precursor films (black) and photonic cured films (red). In (**a**) the open circles represent experimental data, the solid line represents the fitted curves, the green-shaded region is associated with the metal hydroxide contribution and the magenta-shaded region is associated with the metal oxide contribution.

Cross-sectional TEM and STEM were performed to reveal the hybrid TCE structure. Hybrid TCE lamella for TEM and STEM evaluation were prepared using FIB technique. Detailed information on sample preparation and imaging procedure is given in the experimental section and in the supplementary material. Figure 4 shows (a) HAADF image and the corresponding XEDS images for (b) Ag, (c) In, (d) Zn, and (e) O. The AgNWs show up bright in the HAADF image due to high atomic number. Their diameters are approximately 25 nm (Supplementary Figure S7a), in agreement with SEM results in Supplementary Figure S1. The IZO coating forms a uniform layer over the AgNWs and two coats resulted in a thickness of 70 nm for this sample (Supplementary Figure S7b). The interface between the two layers of IZO can be seen in the HAADF image, revealing that one layer of IZO barely covers the AgNWs. Two layers of IZO are needed to overcoat the AgNWs to produce smooth surface, as shown in Figure 2c,d and AFM images (Supplementary Figure S4). The distributions of In and Zn are uniform, with the In:Zn atomic ratio estimated to be 95.5:4.5, consistent with XPS results.
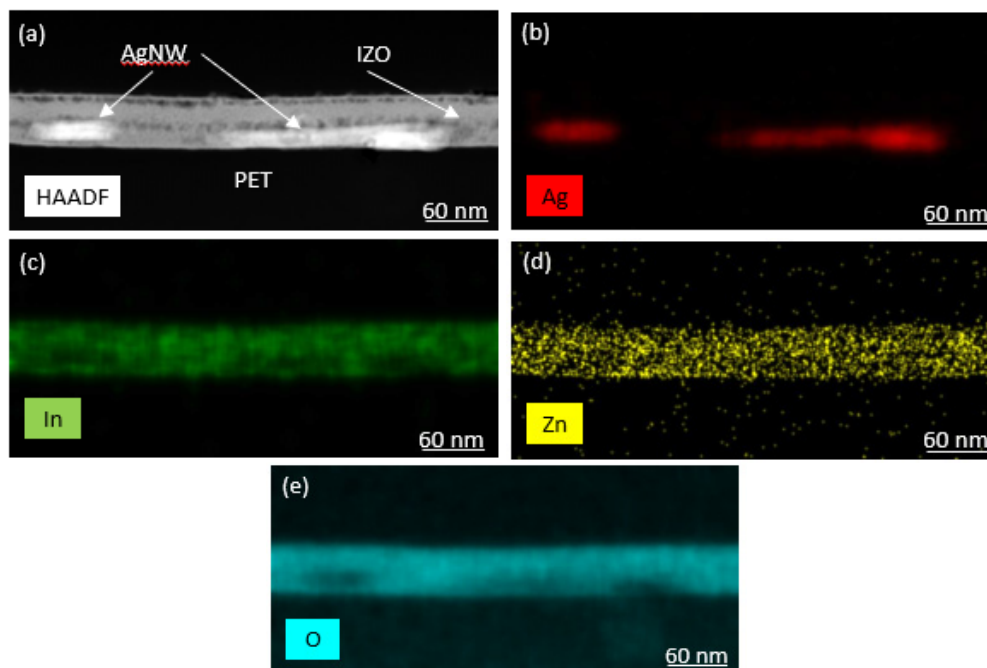

Figure 4. Cross-sectional TEM of a hybrid TCE lamella taken from a location without MBL: (**a**) HAADF STEM and XEDS images for (**b**) Ag, (**c**) In, (**d**) Zn, and (**e**) O taken on the same lamella. AgNWs show up bright in HAADF and Ag images, but dark in In, Zn, and O images.

Hybrid TCE thickness (d) was determined by removing parts of MBL or TCE to expose the bare PET and then the height difference between TCE and PET is measured using an optical profilometer. Examples of thickness measurements are given in Supplementary Figure S8. We find the TCE thickness $d = (80 \pm 10)$ nm. The value of d determined in the cross-sectional TEM image is also in line with these results.

To demonstrate the uniformity of conductivity in hybrid TCE, we applied a bias voltage (~2 V) across the 1 in × 3 in substrates and used an IR thermal camera to observe the temperature rise due to Joule heating. We compare the PET/MBL substrate and the final hybrid TCE sample in Supplementary Figure S9. A schematic of each is shown in Supplementary Figure S9a,d, respectively. Comparing Supplementary Figure S9b,c confirms that the hybrid TCE provides uniform conductivity across the sample, which is critical for collecting photogenerated charges in PSCs. The areal coverage of the AgNWs, defined by the total area covered by AgNWs divided by the total area, was measured to be (28 ± 5)% using SEM images. A representative SEM image before and after processing (filtering) using ImageJ is given in Supplementary Figure S10.

To evaluate the performance of the hybrid TCE compared to other commercially available PET/TCE products, we use the figure-of-merit (FOM), Equation (1) [49–51]. This FOM is based on the ratio of the direct conductivity, $\sigma_{DC} = (R_{sh} \cdot t)^{-1}$, to the optical conductivity, σ_{OP}.

$$FOM = \frac{\sigma_{DC}}{\sigma_{OP}} = \frac{188.5}{R_{sh}\left(T_{avg}^{-1/2} - 1\right)} \tag{1}$$

Table 1 contains the measured T_{avg}, R_{sh}, and the calculated FOM values for our hybrid TCE and two commercially available PET/TCE substrates. Our hybrid TCE is labeled as PET/MBL/AgNW/IZO. The other two samples are Optical Filters (OF) AG12, consisting of a PET/IMI structure [52], and Sigma-Aldrich (SA) PET/ITO [6]. Since the PET substrates used by commercial vendors can have different transmittance due to coating materials and are unknown to us, T_{avg} referenced to air is used for direct comparison here. The hybrid TCE developed in this work has a slightly lower FOM than OF AG12 and a much larger FOM than SA PET/ITO. The calculated FOM for OF AG12 is higher than our hybrid TCE due to the higher T_{avg} and lower R_{sh}. The SA PET/ITO has a much higher R_{sh} compared to the other two substrates, leading to a much lower FOM value. Figure 5 compares the ultraviolet-visible-near infrared (UV-vis-NIR) spectra for the three substrates. The OF AG12 substrate shows short-period interference, while the SA PET/ITO has long-period interference, suggesting that they consist of layers of different materials with thicknesses comparable to the wavelength. The hybrid TCE does not have any observable interference because nanometer-scale materials do not cause interference in this wavelength range.

Table 1. PET/TCE Performance Comparison.

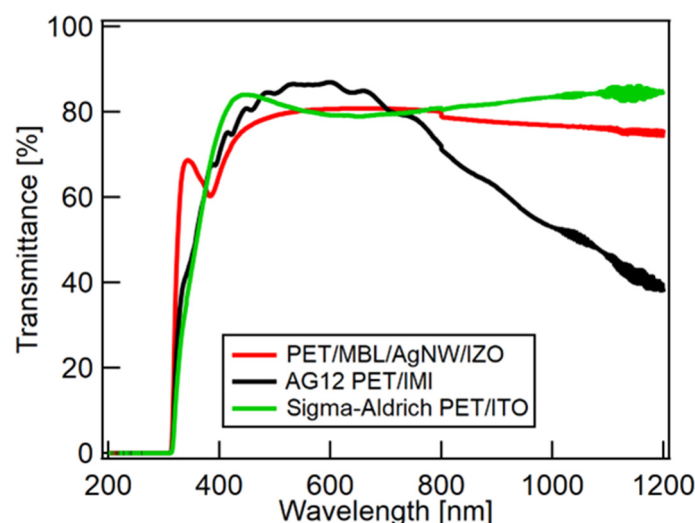| Sample	Vendor	T_{avg} [%]	R_{sh} [Ω sq^{-1}]	FOM	$T_{avg,NIR}$ [%]	FOM$_{NIR}$
PET/MBL/AgNW/IZO	Hsu lab	81 ± 0.4	11 ± 0.5	159 ± 9	78	130
AG12 PET/IMI	Optical Filters	83 ± 0.2	10 ± 0.2	190 ± 4	68	89
PET/ITO	Sigma-Aldrich	81 ± 0.1	72 ± 8.2	24 ± 3	82	25

Figure 5. UV-Vis-NIR transmission spectra, referenced to air, for the three PET/TCE substrates investigated in this work. The discontinuity at ~800 nm results from detector change-over in the measurement tool.

So far, T_{avg} is calculated in the visible range, from 400 to 700 nm. When considering the near-infrared (NIR) and averaging T from 400 to 1200 nm ($T_{avg,NIR}$), we find that OF AG12 has the lowest $T_{avg,NIR}$ and R_{sh}, and SA PET/ITO has the highest $T_{avg,NIR}$ and R_{sh} among the three. The lower optical transmittance of the OF AG12 substrate in the NIR range is due to free carrier absorption, as evidenced by its low R_{sh}. In contrast, the SA PET/ITO substrate has much higher R_{sh}, and thus the optical transmittance in the NIR range is much higher. Because R_{sh} of our hybrid TCE films are determined from AgNW properties and not the IZO layer, it can simultaneously achieve high optical transmittance in the NIR while having low R_{sh}, comparable to OF AG12. Table 1 includes FOM_{NIR} calculated using Equation (1) with $T_{avg,NIR}$ substituting for T_{avg}. For applications where NIR light transmittance is important such as solar cells, our hybrid TCE outperforms both commercially available PET/TCE substrates.

To demonstrate the hybrid TCE can be conveyed over a 2-in roller in device fabrication using R2R, bending tests were completed on three separate samples. Hybrid TCEs were clamped in the upper and lower crossheads as shown in Supplementary Figure S11. Information on the experimental setup and the bending tests are given in the experimental section and supplementary material. Two indium dots were placed 2 in apart on the hybrid TCE, and two-point resistance (R) was measured using a handheld multimeter every 200 cycles. Indium dots decrease the contact resistance between the multimeter probes and the surface of the hybrid TCEs. Initial resistance was measured before any bending cycles (R_0). Figure 6 shows R/R_0 vs. bending cycles. One of the hybrid TCE samples had a 3% increase in resistance after 2000 bending cycles (black dotted/dashed line and circles), while the other two samples only increased by 1%. The minimal increase in resistance after 2000 cycles of bending to 1 in radius demonstrates the hybrid TCE can be conveyed in an R2R setup without degradation.
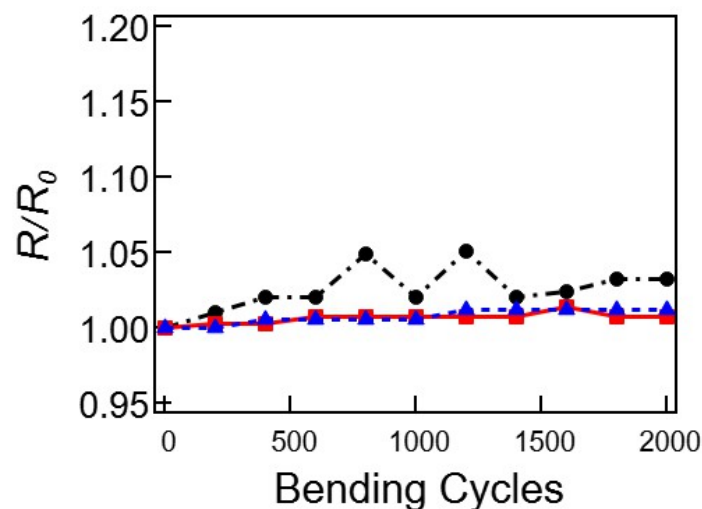

Figure 6. $R/R0$ as a function of bending cycles for three hybrid TCEs at 1 in bending radius for 2000 cycles. Different line styles and markers represent different hybrid TCE samples. The two outlier data points at 800 and 1200 cycles for the black dotted line and circles are attributed to extra contact resistance and do not indicate a true increase in resistance from bending.

3.3. Scaling Up to Large Area

For R2R processing to be cost-effective, the coating and processing must be scaled up. To demonstrate that the hybrid TCE can be scaled up, we performed blade-coating on 7 in × 8 in substrates to fabricate large-area hybrid TCEs and characterize their uniformity. During scale-up, the blade-coating conditions were modified, as described in the experimental section, to yield a uniform film across the large-area substrate. The large-area samples were photonic cured on an R2R tool, shown in the Supplementary Figure S12. Figure 7a shows an image of a large-area hybrid TCE after all processing was completed. The uniformity and control of blade coating are demonstrated by measuring optical and electrical properties at nine locations across the entire sample area, Figure 7b. The average value and relative standard deviation in T_{avg}, R_{sh}, σ_{rms} and d across the entire sample area are 80% ± 0.6% referenced to air (89% ± 0.6% referenced to PET), 24 Ω sq^{-1} ± 13%, 5.9 nm ± 12%, and 64 nm ± 11%, respectively, demonstrating excellent uniformity. While uniformity is excellent, R_{sh} is roughly double compared to the small-area samples. We believe that further optimization of the AgNW blade-coating deposition and photonic curing parameters will produce better results. While the process conditions/parameters used to fabricate

small-area and large-area samples were similar, the environment, equipment, and tools used were different which could result in process and property differences.
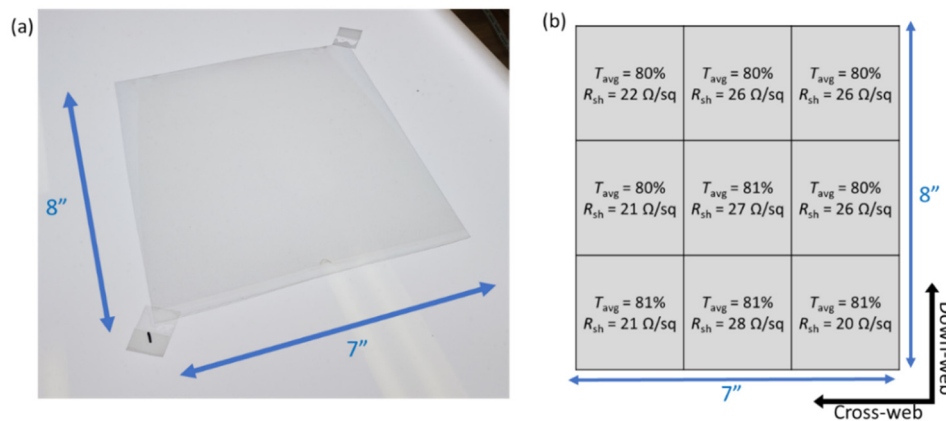

Figure 7. Large-area hybrid TCE: (**a**) Image of 7 in × 8 in large-area hybrid TCE after all processing is complete. (**b**) T_{avg} (referenced to air) and R_{sh} measurements at nine locations across the large-area hybrid TCE samples.

3.4. Optimizing Photonic Curing to Increase R2R Web Speed

Thus far, the hybrid TCEs have been made using photonic curing conditions with 9 pulses. The number of photonic curing pulses directly affects the highest achievable R2R web speed, as shown in Equation (2) [15].

$$s = \frac{f \cdot w}{0.2 \cdot N \cdot o} \tag{2}$$

This equation shows how the web speed (s, ft min^{-1}), depends on the repetition rate (f, Hz), number of pulses (N), overlap factor (o), and down web lamp dimension (w, which is 3 in for our system). The overlap factor is to compensate for the intensity of the lamp pulse drops off near the edges of the illumination area. A value of 1.2 is recommended by PulseForge, which produces 17% overlap between subsequent pulses and ensures uniform pulse intensity down web. The repetition rate depends on the photonic curing condition and equipment (lamp type, number of lamp drivers, and power supply current output) [15,26,27,31]. The repetition rate is calculated, based on the pulse conditions and tool configuration, by the PulseForge tool's software. The power supply recharges the lamp drivers between pulses with a fixed current output [27], and its capacity has the largest impact on the repetition rate. The power supply for the UTD photonic curing tool is 1.5 kW. The web speed of the 9-pulse condition using this tool is 0.14 m min^{-1}, two orders of magnitude slower than the typically target R2R web speed of 10 m min^{-1}. To achieve faster web speeds, the number of pulses should be reduced. Additionally, reducing the number of photonic curing pulses will decrease the time to fabricate the hybrid TCE, directly translating to lower electricity usage and lower carbon emissions. Hence, we aim to find photonic curing conditions that can produce the hybrid TCE with a single pulse.

Latin Hypercube sampling (LHS) was employed to find photonic curing parameters with a single pulse. To find the optimal conditions, the following photonic curing parameters were varied: fluence (1.5–5 J cm^{-2} with step of 0.2 J cm^{-2}), pulse length (5–30 ms with step of 1 ms), number of micro-pulses (2–30 with step of 1), and duty cycle (20–70% with step of 5%). The number of pulses was fixed to one, and the fluence was controlled by adjusting the lamp voltage. The photonic curing conditions used for experiments are shown in Supplementary Table S1. The goal is to find a 1-pulse condition that produces a hybrid TCE similar to the 9-pulse condition. We use transmittance below 400 nm, where IZO is absorbing, as the metric, because that part of the spectrum is sensitive coating and processing, e.g., see Supplementary Figure S2. Figure 8a shows UV-Vis transmittance spectra for hybrid TCEs fabricated by photonic curing with the 9-pulse condition (red), LHS condition 4 (blue), LHS condition 15 (orange), and LHS condition 19 (green). Figure 8a shows that when a hybrid TCE is made with the 9-pulse condition it has one peak in the spectrum between 320 and 400 nm. When analyzing the UV-Vis transmittance of hybrid TCEs made with different LHS conditions, only a few conditions produce a similar shape as the 9-pulse condition, i.e., only one peak. Figure 8a shows LHS conditions 15 and 19 which have two peaks in this spectral region, while LHS condition 4 matches closely with the 9-pulse condition. To quantify the shape similarity, Procrustes distance was calculated between the two transmittance curves, 9-pulse hybrid TCE and a hybrid TCE made with a specific LHS photonic curing condition, in the range 330–390 nm. Procrustes analysis facilitates the extraction of meaningful information about the shape similarity between curves while eliminating

differences unrelated to shape, such as rigid translations or rotations [53]. Further details on the Procrustes analysis are given in the supplementary material. A smaller Procrustes distance means a better match between the curves. The Procrustes distances for all the LHS conditions are given in Supplementary Table S1. LHS condition 4 (LHS4) has the smallest Procrustes distance, consistent with Figure 8a. LHS4 photonic curing parameters are 330 V lamp voltage, 10 ms pulse length, 24 micro-pulses, 65% duty cycle, and 3.6 J cm^{-2} fluence. Because this is a single pulse process, the total processing time is only 10 ms. The calculated web speed of the LHS4 condition, using Equation (2), is 1.6 m min^{-1} using the UTD tool, which is ~10 times faster than the 9-pulse condition. Henceforth, LHS4 will be referred to as the 1-pulse condition.

XPS analysis was performed to further compare the hybrid TCEs made with the 9-pulse versus 1-pulse conditions. Figure 8b,c show XPS spectra of O 1s and N 1s, respectively, comparing hybrid TCEs made with 9-pulse (red) and 1-pulse (blue) photonic curing processes. The XPS spectra for the Ag 3d, In 3d, and Zn 2p are given in the Supplementary Figure S13. Both samples contained a layer of AgNWs and one coat of IZO. The O 1s spectra also show nearly identical metal hydroxide (green shaded region, 532 eV binding energy) and metal oxide (pink shaded region, 530 eV binding energy) components for both photonic curing processes (Figure 8c). The N 1s spectra for each process show a significant reduction of nitrate species signals (~ 407 eV binding energy) from the precursor (Figure 8c black curve), indicating the successful breakdown of metal nitrate salts in the precursor solution to metal hydroxide and oxide species. These results indicate that both photonic curing processes can produce similar IZO conversion results.
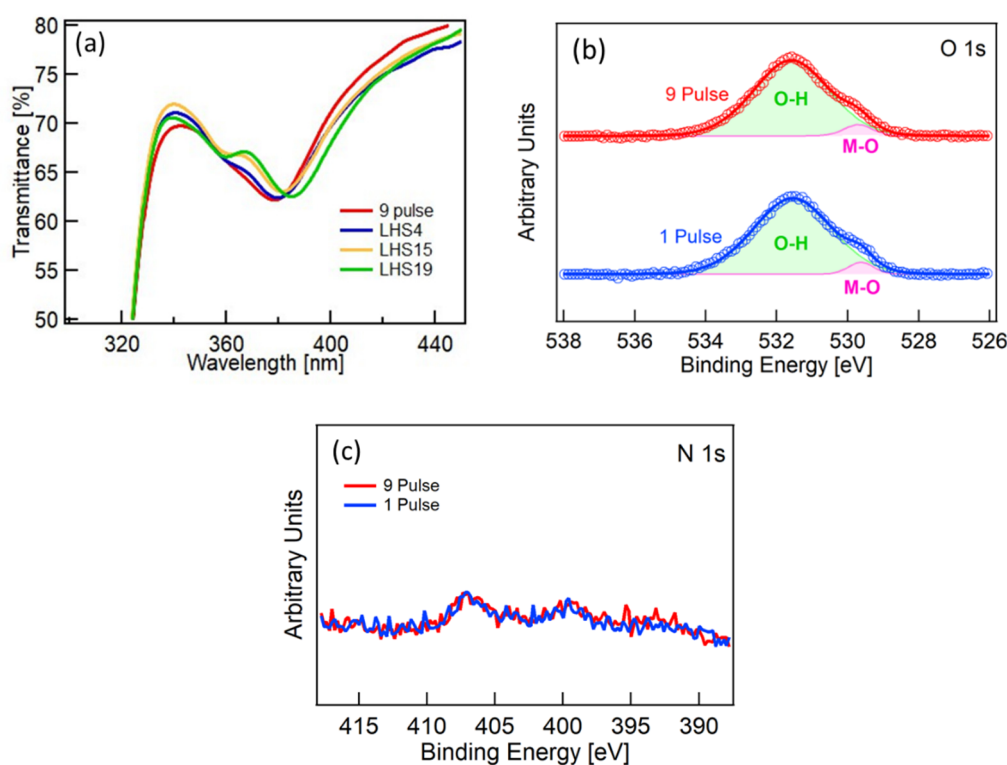

Figure 8. UV-Vis and XPS for 9-pulse vs 1-pulse photonic curing conditions: (**a**) UV-Vis spectra for hybrid TCEs made with 9-pulse photonic curing condition (red) and three different LHS conditions (blue, orange, and green). XPS spectra for (**b**) O 1s and (**c**) N 1s comparing 9-pulse (red) and the LHS4 condition (blue). In (**b**) the open circles represent experimental data, the solid line represents the fitted curves, the green-shaded region is associated with the metal hydroxide contribution, and the magenta-shaded region is associated with the metal oxide contribution.

Overall, hybrid TCEs made using the 1-pulse condition have an average T_{avg} of (81 ± 1.0)% referenced to air $((90 \pm 0.9)$% referenced to PET), $R_{sh} = (10 \pm 1.3)\ \Omega$ sq^{-1}, and $d = (78 \pm 16)$ nm. Similar results in electrical, optical, physical, and chemical properties for materials produced in 1-pulse condition compared to 9-pulse condition enable us to increase web speed tenfold. Using a more powerful photonic curing tool at PulseForge equipped with a 15 kW power supply, the repetition rate can be increased to achieve a web speed of 11 m min^{-1} when using the 1-pulse condition.

3.5. Performance of Perovskite Solar Cells on Hybrid TCEs

Perovskite solar cells are made to validate the TCE performance. *P-i-n* device architecture was used, composed of the following layers from bottom to top: PET/hybrid TCE/hole transport layer (HTL)/MAPbI/PCBM/BCP/Al/Ag. Full PSC fabrication details are given in the method section. The HTL consists of a layer of neutral pH PEDOT:PSS, deposited on top of the hybrid TCE, followed by a layer of regular PEDOT:PSS, and a layer of self-assemble molecules (SAMs, MeO-2PACz). Supplementary Figure S14 shows the transmittance spectra of the hybrid TCE after the sequential deposition of neutral PEDOT:PSS, neutral PEDOT:PSS/ PEDOT:PSS, neutral PEDOT:PSS/ PEDOT:PSS/MeO-2PACz. A schematic of the device stack is given in Figure 9a. The neutral pH PEDOT:PSS was made by adding ammonium hydroxide to the regular PEDOT:PSS solution (see experimental section) and has a pH of 7, in contrast to pH of 1.7 for the regular PEDOT:PSS. The neutral PEDOT:PSS minimizes the etching of IZO by the regular PEDOT:PSS [54]. The deposition of MeO-2PACz on top of the PEDOT:PSS bilayer affects the morphology and crystal quality of the $MAPbI_3$ layer. The non-wetting property of MeO-2PACz reduces the dragging force between the HTL surface and the $MAPbI_3$ precursor during spin coating, which lowers the density of perovskite nucleation sites, leading to larger grain size and fewer defects in $MAPbI_3$ films [55,56].

PSCs were fabricated on top of 9-pulse and 1-pulse processed hybrid TCEs. The champion *J-V* curves for forward and reverse scans are given in Figure 9b, showing little hysteresis, and box plots of the average *J-V* parameters are given in Figure 9c. Devices made on both 9-pulse and 1-pulse hybrid TCEs resulted in similar performance, further indicating that the 1-pulse photonic curing conditions can successfully make high-performing hybrid TCEs. The champion power conversion efficiency (PCE) for PSCs made on the 9-pulse and 1-pulse hybrid TCEs were 11.4% and 10.7%, respectively. Table 2 shows that the average *J-V* parameters for PSC devices made on 9-pulse and 1-pulse hybrid TCEs are statistically equivalent. Additionally, these average and champion PCE values are ~ 50% higher than the same devices fabricated on SA PET/ITO substrates (Supplementary Figure S15 and Supplementary Table S2) because of the superior properties of our hybrid TCEs, as discussed in Section 3.2.
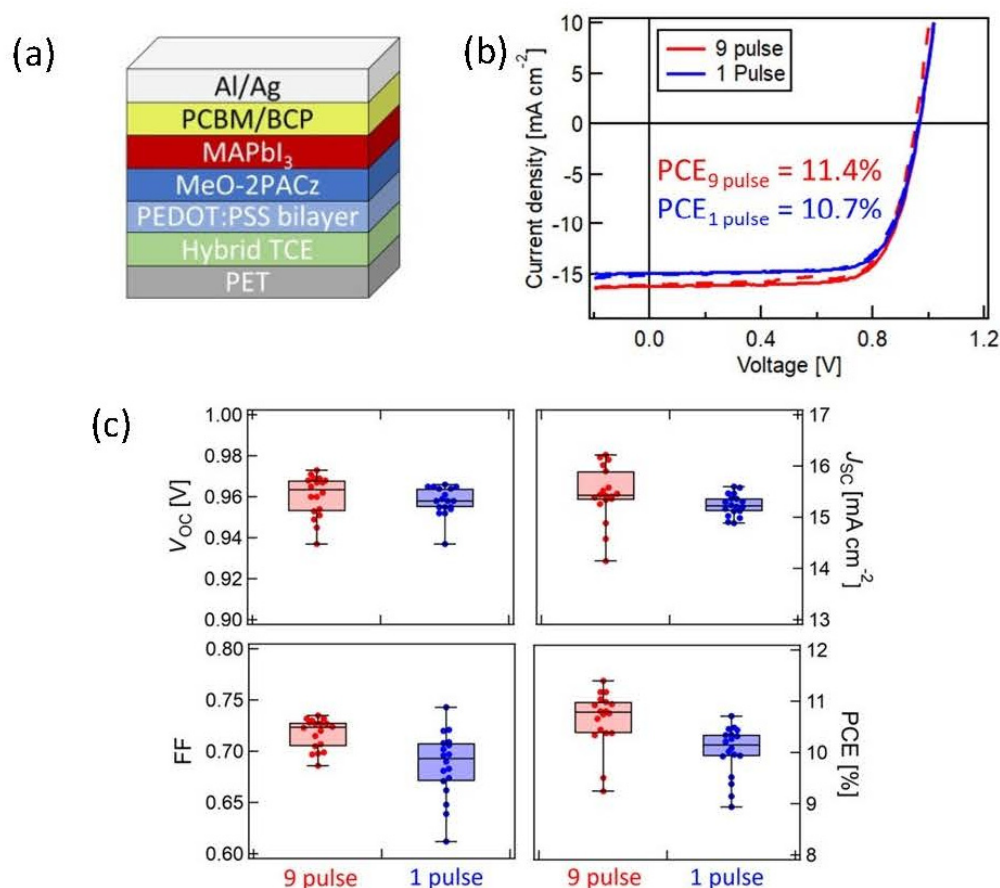

Figure 9. Performance of PSC devices made on 9-pulse vs 1-pulse fabricated hybrid TCEs: (**a**) Schematic *p-i-n* PSC device structure. (**b**) Champion *J-V* forward (dashed) and reverse (solid) curves and (**c**) box plot of *J-V* parameters for PSCs made on hybrid TCEs photonic cured with 9-pulse and 1-pulse conditions. The bottom and

top of the boxes represent the 25th and 75th percentiles, the middle line is the median, and the whiskers extend to the minimum and maximum values.

Table 2. Average and champion *J-V* results for PSCs fabricated on top of hybrid TCEs made with 9-pulse and 1-pulse photonic curing conditions.

TCE Photonic Curing Condition	V_{oc} [V]	J_{sc} [mA cm^{-2}]	FF	Average PCE [%]	Champion PCE [%]
9-pulse	0.960 ± 0.01	15.5 ± 0.54	0.717 ± 0.02	10.7 ± 0.55	11.4
1-pulse	0.958 ± 0.01	15.2 ± 0.21	0.687 ± 0.03	10.0 ± 0.49	10.7

To demonstrate that the hybrid TCEs can be made at a web speed greater than 10 m min^{-1}, stitching mode was employed to fabricate four hybrid TCEs in a single process. In stitching mode, the photonic curing stage moves underneath the flash lamp at a fixed web speed, while the stationary flash lamp pulses at a fixed repetition rate. Because blade coating must be done at UTD while the photonic curing was performed at PulseForge (Austin, TX), sample preparation for hybrid TCEs made at 11 m min^{-1} was different than for the hybrid TCEs made one by one at UTD. Four samples that have two coats of dried IZO layers were secured to the photonic curing stage with Kapton tape and labeled based on positions A, B, C, and D as shown in Figure 10. More information on sample preparation is given in the supplementary material. The samples were photonic cured with the 1-pulse condition in stitching mode at 11 m min^{-1}. T_{avg} and R_{sh} were measured at two locations on each of the four sample positions. PSC devices were fabricated on the hybrid TCE samples made at positions A-D. These samples will henceforth be referred to as stitching samples. Three batches of stitching samples were made to assess process repeatability. The average results for all the stitching samples are given in Table 3. Both batch-to-batch and positional variation were low, indicating good process control. The down web uniformity across the four positions was good, with the overall average and relative standard deviation being 76% $\pm$ 1.5% referenced to air (85% $\pm$ 1.4% referenced to PET) and 9.2 Ω sq^{-1} $\pm$ 8.0% for T_{avg} and R_{sh}, respectively. Hybrid TCE *d* made in stitching mode was measured to be 100 ± 22 nm. The reduced transmittance and increased *d* are attributed to the difference in sample preparation.

The uniformity of hybrid TCEs was further demonstrated by PSC PCE overall average and relative standard deviation being (10.5 $\pm$ 1.0)% across the four positions. The PCE average and standard deviation based on sample position are given in Table 3. Figure 11a shows champion *J-V* curves for PSCs made on stitching samples at each position. Supplementary Figure S16 provides an example *J-V* curves of these devices showing low hysteresis between forward and reverse scans. Figure 11b shows box plots for average *J-V* parameters indicating similar performance across each sample position. Hence, photonic curing at a web speed of 11 m min^{-1} to fabricate hybrid TCEs has been successfully demonstrated.
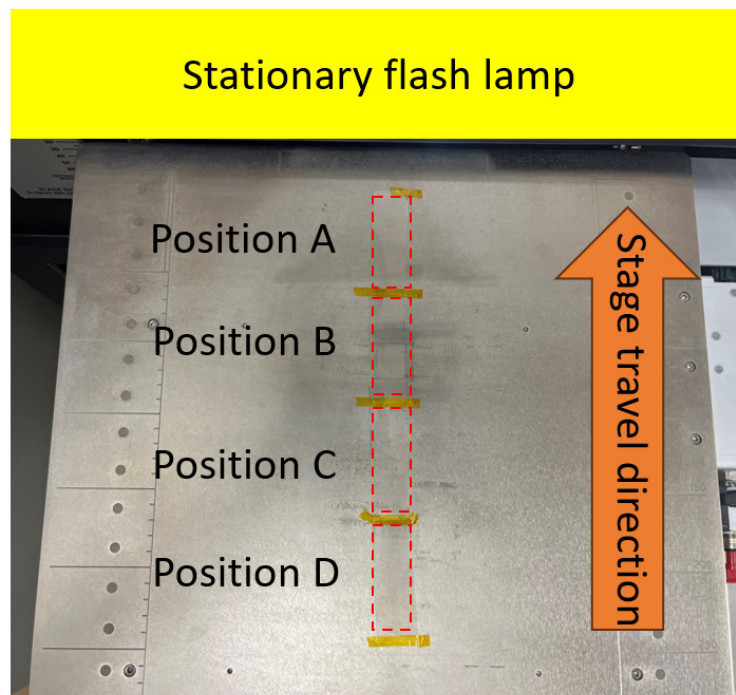
Figure 10. Photograph of samples on the photonic curing stage for stitching experiments. Sample positions A–D and stage travel direction under the stationary xenon flash lamp (yellow box) are labeled.

Table 3. Average T_{avg} (referenced to air) and R_{sh}, of hybrid TCEs made by stitching and average PCE for PSCs made on top of the stitching samples.

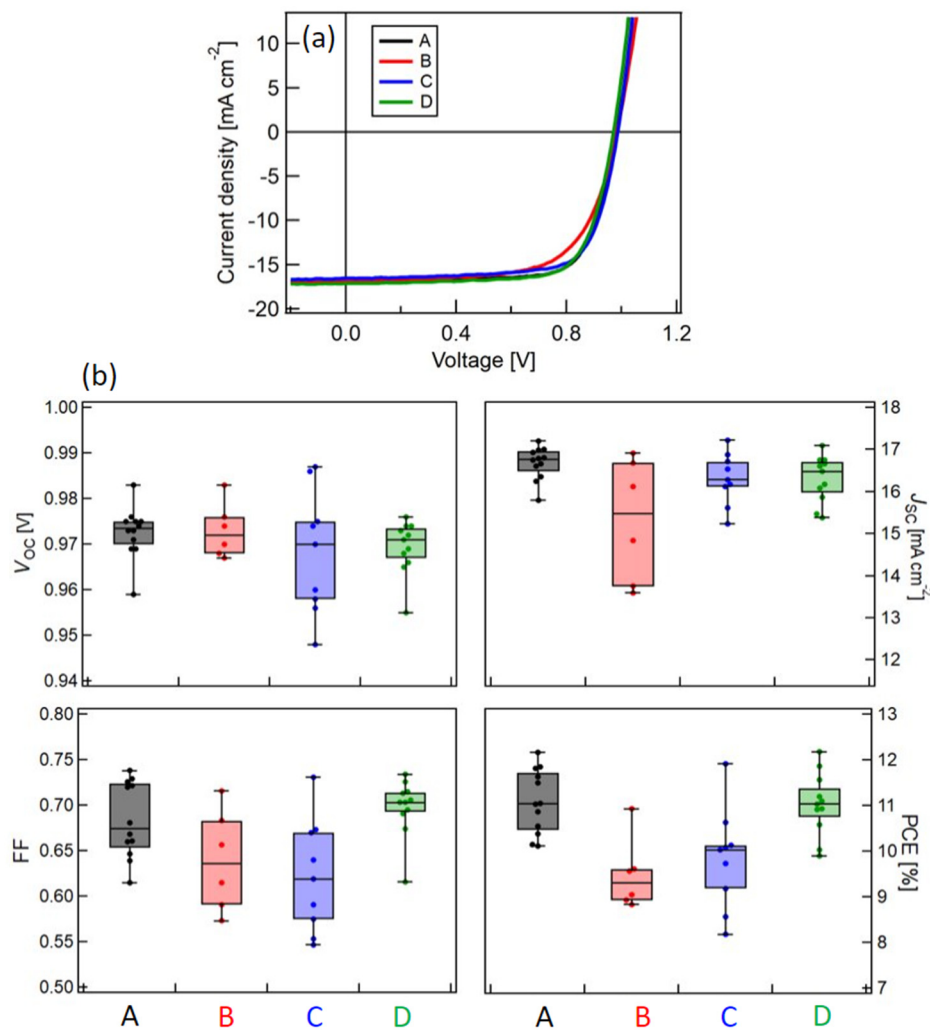| Position	T_{avg} (%)	R_{sh} (Ω sq^{-1})	Average PCE (%)
A	76 ± 0.6	9.0 ± 0.7	11.1 ± 0.70
B	76 ± 0.6	9.0 ± 0.7	9.50 ± 0.78
C	77 ± 1.2	9.6 ± 0.8	9.83 ± 1.1
D	75 ± 2.1	9.0 ± 0.6	11.0 ± 0.69

Figure 11. Characteristics of PSC devices made on hybrid TCEs made by photonic curing in stitching mode at 11 m min^{-1}: (**a**) Champion *J-V* reverse curves and (**b**) box plot comparing the average *J-V* parameters of the PSCs on hybrid TCEs positioned at A (black), B (red), C (blue), and D (green) as illustrated in Figure 10 and photonic cured at 11 m min^{-1}. The bottom and top of the boxes represent the 25th and 75th percentiles, the middle line is the median, and the whiskers extend to the minimum and maximum values.

4. Conclusions

In conclusion, we demonstrate hybrid TCEs with excellent optoelectronic properties on PET substrates made by blade-coating and photonic curing in ambient environment: T_{avg} = (81 ± 0.4)% referenced to air (90 ± 0.4 % referenced to PET), R_{sh} = (11 ± 0.5) Ω sq^{-1}, and σ_{rms} = (4.3 ± 0.4) nm. The hybrid TCE structure consists of a multiscale Ag network of MBLs and AgNWs overcoated by an IZO layer. XPS results showed that the photonic curing efficiently decomposes nitrate in milliseconds and initiates the conversion from precursors to IZO films. Compared to two commercially available PET/TCE products, our hybrid TCEs perform similarly or better in the visible range and outperform these products when near IR transmission is considered. The superior performance of the hybrid TCEs is further validated by PSC devices, which show 50% higher PCEs when made on our hybrid TCEs than on commercial PET/ITO substrates. The hybrid TCE fabrication process was scaled up to make large-area (7 in × 8 in) samples with similar properties as the small samples and excellent uniformity of <1% in T_{avg}, 13% in R_{sh}, 12% in σ_{rms}, and 11% in *d*. To speed up photonic curing, we identify a 1-pulse condition that can produce hybrid TCEs with properties comparable to those made with the standard 9-pulse condition, as confirmed by T_{avg}, R_{sh}, *d*, XPS, and PSC performance. Reducing the number of pulses down to one increases the web speed tenfold using the same photonic curing tool. Using the 1-pulse condition, hybrid TCEs were photonic cured at 11 m min^{-1} and exhibited a great down web uniformity of T_{avg} (76% ± 1.5%) referenced to air (85% ± 1.4% referenced to PET), and R_{sh} (9.2 Ω sq^{-1} ± 8.0%). PSCs fabricated on these hybrid TCEs had an average and champion PCE of (10.5 ± 1.0)% and 12.2%, respectively. In this work, we demonstrate the fabrication of hybrid TCEs on PET using blade-coating followed by photonic curing processing. While photonic curing is truly compatible with R2R

manufacturing due to its high speed (>10 m min^{-1}), blade coating is not. Future work using solution deposition techniques such as gravure or flexographic printing would make the hybrid TCE fabrication method fully compatible with high throughput R2R manufacturing. In addition to solar cells, these hybrid TCEs can greatly impact other optoelectronic applications such as flexible light-emitting diodes, touch screens, displays, IoT sensors, and transparent heaters. The adaptation of photonic curing to replace thermal annealing reduces energy use and carbon emissions, paving a novel "green" material processing pathway for high-throughput manufacturing.

Supplementary Materials

The following supporting information can be downloaded at: https://www.sciltp.com/journals/matsus/2025/1/530/s1, Figure S1. SEM micrographs of AgNWs; Figure S2. UV-Vis transmission of hybrid TCE; Figure S3. MBL damage after photonic curing; Figure S4. AFM images and height profiles of hybrid TCE; Figure S5. Normalized XPS spectra of precursor and final hybrid TCE; Figure S6. TGA of indium and zinc precursor salts; Figure S7. TEM and STEM cross section images of hybrid TCE; Figure S8. Hybrid TCE thickness measurements using Keyence VK-X3100; Figure S9. IR images of hybrid TCE; Figure S10. AgNW coverage; Figure S11. Bending testing equipment setup; Figure S12. R2R photonic curing tool; Table S1. LHS conditions; Figure S13. Normalized XPS spectra of hybrid TCE made with 9-pulse vs. 1-pulse; Figure S14. UV-Vis transmittance of hybrid TCE. and HTL; Figure S15. J-V results for hybrid TCE and PET/ITO; Table S2: Average J-V parameters along with champion PCE of the PSCs on hybrid TCEs and PET/ITO. Figure S16. Champion PSC J-V curves for stitching samples.

Author Contributions

J.C.B. and R.T.P.: writing—original draft, writing—review and editing, methodology, formal analysis, investigation, validation, data curation, visualization: these two authors contributed equally. B.B.: writing—original draft, investigation, validation, data curation, formal analysis. C.R.A.: formal analysis. C.T.B., M.A.O., M.D., and M.V.: investigation. M.L.: writing—review and editing, conceptualization, supervision. J.W.P.H.: writing—original draft, writing—review and editing, conceptualization, supervision, project administration, funding acquisition, methodology, resources. All authors have read and agreed to the published version of the manuscript.

Funding

Data Availability Statement

The datasets generated during and/or analyzed during the current study are available from the corresponding author upon reasonable request. Statistical reporting is included when data are presented.

Acknowledgments

Disclaimer

This report was prepared as an account of work sponsored by an agency of the United States Government. Neither the United States Government nor any agency thereof, nor any of their employees, makes any warranty, express or implied, or assumes any legal liability or responsibility for the accuracy, completeness, or usefulness of any information, apparatus, product, or process disclosed, or represents that its use would not infringe privately owned rights. Reference herein to any specific commercial product, process, or service by trade name, trademark, manufacturer, or otherwise does not necessarily constitute or imply its endorsement, recommendation, or favoring by the United States Government or any agency thereof. The views and opinions of authors expressed herein do not necessarily state or reflect those of the United States Government.

Conflicts of Interest

All authors declare no financial or non-financial conflict of interest.

References

1. Nguyen, V.H.; Papanastasiou, D.T.; Resende, J.; et al. Advances in Flexible Metallic Transparent Electrodes. *Small* **2022**, *18*, 2106006. https://doi.org/10.1002/smll.202106006.

2. McLellan, K.; Yoon, Y.; Leung, S.N.; et al. Recent Progress in Transparent Conductors Based on Nanomaterials: Advancements and Challenges. *Adv. Mater. Technol.* **2020**, *5*, 1900939. https://doi.org/10.1002/admt.201900939.

3. Ellmer, K. Past Achievements and Future Challenges in the Development of Optically Transparent Electrodes. *Nat. Photonics* **2012**, *6*, 809–817. https://doi.org/10.1038/nphoton.2012.282.

4. Zhang, Y.; Ng, S.W.; Lu, X.; et al. Solution-Processed Transparent Electrodes for Emerging Thin-Film Solar Cells. *Chem. Rev.* **2020**, *120*, 2049–2122. https://doi.org/10.1021/acs.chemrev.9b00483.

5. Lee, M.; Piper, R.T.; Bhandari, B.; et al. Multiobjective Optimization of Silver-Nanowire Deposition for Flexible Transparent Conducting Electrodes. *ACS Appl. Nano Mater.* **2023**, *6*, 17364–17368. https://doi.org/10.1021/acsanm.3c03599.

6. Sigma, M. Indium Tin Oxide Coated PET Available online: https://www.sigmaaldrich.com/US/en/product/aldrich/639303 (accessed on 1 June 2023).

7. Laghrib, S.; Benhaliliba, M.; Adnani, H.; et al. Wide Bandgap Indium-Doped SnO_2 Semiconductor Prepared by Sol-Gel Route: Multilayer Fabrication and Low Resistivity for Solar Cell Application. *J. Sol-Gel Sci. Technol.* **2023**, *106*, 530–544. https://doi.org/10.1007/s10971-023-06093-y.

8. Fan, X. Doping and Design of Flexible Transparent Electrodes for High-Performance Flexible Organic Solar Cells: Recent Advances and Perspectives. *Adv. Funct. Mater.* **2021**, *31*, 2009399. https://doi.org/10.1002/adfm.202009399.

9. Lu, X.; Zhang, Y.; Zheng, Z. Metal-Based Flexible Transparent Electrodes: Challenges and Recent Advances. *Adv. Electron. Mater.* **2021**, *7*, 2001121. https://doi.org/10.1002/aelm.202001121.

10. Lee, H.B.; Jin, W.Y.; Ovhal, M.M.; et al. Flexible Transparent Conducting Electrodes Based on Metal Meshes for Organic Optoelectronic Device Applications: A Review. *J. Mater. Chem. C* **2019**, *7*, 1087–1110. https://doi.org/10.1039/c8tc04423f.

11. Azani, M.; Hassanpour, A.; Torres, T. Benefits, Problems, and Solutions of Silver Nanowire Transparent Conductive Electrodes in Indium Tin Oxide (ITO)-Free Flexible Solar Cells. *Adv. Energy Mater.* **2020**, *10*, 2002536. https://doi.org/10.1002/aenm.202002536.

12. Parente, M.; Van Helvert, M.; Hamans, R.F.; et al. Simple and Fast High-Yield Synthesis of Silver Nanowires. *Nano Lett.* **2020**, *20*, 5759–5764. https://doi.org/10.1021/acs.nanolett.0c01565.

13. Energy, U.D. Of Energy Earthshots—U.S. Department of Energy Industrial Heat Shot. Available online: https://www.energy.gov/sites/default/files/2022-09/earth-shot-industrial-heat-fact-sheet.pdf (accessed on 24 September 2024).

14. Schroder, K.A. Mechanisms of Photonic Curing™: Processing High Temperature Films on Low Temperature Substrates. In Proceedings of the Technical Proceedings of the 2011 NSTI Nanotechnology Conference and Expo, Boca Raton, FL, USA, 13–16 June 2011; pp. 220–223.

15. Schroder, K.A.; Martin, K.M.; Jackson, D.K.; et al. Method and Apparatus for Curing Thin Films on Low-Temperature Substrates at High Speeds 2013. U.S. Patent 9, 095, 874 B2, 4 August 2014.

16. Gerlein, L.F.; Benavides-Guerrero, J.A.; Cloutier, S.G. High-Performance Silver Nanowires Transparent Conductive Electrodes Fabricated Using Manufacturing-Ready High-Speed Photonic Sinterization Solutions. *Sci. Rep.* **2021**, *11*, 24156. https://doi.org/10.1038/s41598-021-03528-w.

17. Piper, R.T.; Xu, W.; Hsu, J.W.P. Silver Nanowire-Indium Zinc Oxide Composite Flexible Transparent Conducting Electrodes Made by Spin-Coating and Photonic Curing. *MRS Adv.* **2023**, *8*, 177–182. https://doi.org/10.1557/s43580-022-00478-x.

18. Jiu, J.; Nogi, M.; Sugahara, T.; et al. Strongly Adhesive and Flexible Transparent Silver Nanowire Conductive Films Fabricated with a High-Intensity Pulsed Light Technique. *J. Mater. Chem.* **2012**, *22*, 23561–23567. https://doi.org/10.1039/c2jm35545k.

19. Kim, K.S.; Choi, S.B.; Kim, D.U.; et al. Photo-Induced Healing of Stretchable Transparent Electrodes Based on Thermoplastic Polyurethane with Embedded Metallic Nanowires. *J. Mater. Chem. A* **2018**, *6*, 12420–12429. https://doi.org/10.1039/c8ta02979b.

20. Yang, Y.; Ding, S.; Araki, T.; et al. Facile Fabrication of Stretchable Ag Nanowire/Polyurethane Electrodes Using High Intensity Pulsed Light. *Nano Res.* **2016**, *9*, 401–414. https://doi.org/10.1007/s12274-015-0921-9.

21. Schroder, K.A.; McCool, S.C.; Furlan, W.F. Broadcast Photonic Curing of Metallic Nanoparticle Films. In Proceedings of the 2006 NSTI Nanotechnology Conference and Trade Show, Boston, MA, USA, 7–11 May 2006.

22. Akhavan, V.; Schroder, K.; Farnsworth, S. Photonic Curing Enabling High-Speed Sintering of Metal Inkjet Inks on Temperature-Sensitive Substrates. In *Handbook of Industrial Inkjet Printing*; Wiley: Weinheim, Germany, 2017; Volume 2, pp. 557–566, ISBN 9783527687169.

23. Galagan, Y.; Coenen, E.W.C.; Abbel, R.; et al. Photonic Sintering of Inkjet Printed Current Collecting Grids for Organic Solar Cell Applications. *Org. Electron.* **2013**, *14*, 38–46. https://doi.org/10.1016/j.orgel.2012.10.012.

24. Ghahremani, A.H.; Pishgar, S.; Bahadur, J.; et al. Intense Pulse Light Annealing of Perovskite Photovoltaics Using Gradient Flashes. *ACS Appl. Energy Mater.* **2020**, *3*, 11641–11654. https://doi.org/10.1021/acsaem.0c01520.

25. Lavery, B.W.; Kumari, S.; Konermann, H.; et al. Intense Pulsed Light Sintering of CH3NH3PbI3 Solar Cells. *ACS Appl. Mater. Interfaces* **2016**, *8*, 8419–8426. https://doi.org/10.1021/acsami.5b10166.

26. Xu, W.; Daunis, T.B.; Piper, R.T.; et al. Effects of Photonic Curing Processing Conditions on MAPbI 3 Film Properties and Solar Cell Performance. *ACS Appl. Energy Mater.* **2020**, *3*, 8636–8645. https://doi.org/10.1021/acsaem.0c01243.

27. Piper, R.T.; Daunis, T.B.; Xu, W.; et al. Photonic Curing of Nickel Oxide Transport Layer and Perovskite Active Layer for Flexible Perovskite Solar Cells: A Path Towards High-Throughput Manufacturing. *Front. Energy Res.* **2021**, *9*, 76. https://doi.org/10.3389/fenrg.2021.640960.

28. Troughton, J.; Carnie, M.J.; Davies, M.L.; et al. Photonic Flash-Annealing of Lead Halide Perovskite Solar Cells in 1 Ms. *J. Mater. Chem. A* **2016**, *4*, 3471–3476. https://doi.org/10.1039/c5ta09431c.

29. Piper, R.T.; Xu, W.; Hsu, J.W.P. How Optical and Electrical Properties of ITO Coated Willow Glass Affect Photonic Curing Outcome for Upscaling Perovskite Solar Cell Manufacturing. *IEEE J. Photovolt.* **2022**, *12*, 722–727. https://doi.org/10.1109/JPHOTOV.2022.3159395.

30. Das, S.; Gu, G.; Joshi, P.C.; et al. Low Thermal Budget, Photonic-Cured Compact TiO2 Layers for High-Efficiency Perovskite Solar Cells. *J. Mater. Chem. A* **2016**, *4*, 9685–9690. https://doi.org/10.1039/c6ta02105k.

31. Daunis, T.B.; Schroder, K.A.; Hsu, J.W.P. Photonic Curing of Solution-Deposited ZrO$_2$ Dielectric on PEN: A Path towards High-Throughput Processing of Oxide Electronics. *NPJ Flex. Electron.* **2020**, *4*, 7. https://doi.org/10.1038/s41528-020-0070-4.

32. Ghahremani, A.H.; Martin, B.; Gupta, A.; et al. Rapid Fabrication of Perovskite Solar Cells through Intense Pulse Light Annealing of SnO2 and Triple Cation Perovskite Thin Films. *Mater. Des.* **2020**, *185*, 108237. https://doi.org/10.1016/j.matdes.2019.108237.

33. Feleki, B.; Bex, G.; Andriessen, R.; et al. Rapid and Low Temperature Processing of Mesoporous TiO2 for Perovskite Solar Cells on Flexible and Rigid Substrates. *Mater. Today Commun.* **2017**, *13*, 232–240. https://doi.org/10.1016/j.mtcomm.2017.09.007.

34. Martin, B.; Amos, D.; Brehob, E.; et al. Techno-Economic Analysis of Roll-to-Roll Production of Perovskite Modules Using Radiation Thermal Processes. *Appl. Energy* **2022**, *307*, 118200. https://doi.org/10.1016/j.apenergy.2021.118200.

35. Scheideler, W.J.; Smith, J.; Deckman, I.; et al. A Robust, Gravure-Printed, Silver Nanowire/Metal Oxide Hybrid Electrode for High-Throughput Patterned Transparent Conductors. *J. Mater. Chem. C* **2016**, *4*, 3248–3255. https://doi.org/10.1039/C5TC04364F.

36. Lee, E.; Ahn, J.; Kwon, H.C.; et al. All-Solution-Processed Silver Nanowire Window Electrode-Based Flexible Perovskite Solar Cells Enabled with Amorphous Metal Oxide Protection. *Adv. Energy Mater.* **2018**, *8*, 1702182. https://doi.org/10.1002/aenm.201702182.

37. Kim, S.; Kim, S.Y.; Kim, J.; et al. Highly Reliable AgNW/PEDOT:PSS Hybrid Films: Efficient Methods for Enhancing Transparency and Lowering Resistance and Haziness. *J. Mater. Chem. C* **2014**, *2*, 5636–5643. https://doi.org/10.1039/c4tc00686k.

38. Morgenstern, F.S.F.; Kabra, D.; Massip, S.; et al. Ag-Nanowire Films Coated with ZnO Nanoparticles as a Transparent Electrode for Solar Cells. *Appl. Phys. Lett.* **2011**, *99*, 183307. https://doi.org/10.1063/1.3656973.

39. Wu, C.; Jiu, J.; Araki, T.; et al. Rapid Self-Assembly of Ultrathin Graphene Oxide Film and Application to Silver Nanowire Flexible Transparent Electrodes. *RSC Adv.* **2016**, *6*, 15838–15845. https://doi.org/10.1039/c5ra24896e.

40. Lee, J.Y.; Connor, S.T.; Cui, Y.; et al. Solution-Processed Metal Nanowire Mesh Transparent Electrodes. *Nano Lett.* **2008**, *8*, 689–692. https://doi.org/10.1021/nl073296g.

41. Lu, H.; Sun, J.; Zhang, H.; et al. Room-Temperature Solution-Processed and Metal Oxide-Free Nano-Composite for the Flexible Transparent Bottom Electrode of Perovskite Solar Cells. *Nanoscale* **2016**, *8*, 5946–5953. https://doi.org/10.1039/C6NR00011H.

42. Chen, X.; Xu, G.; Zeng, G.; et al. Realizing Ultrahigh Mechanical Flexibility and >15% Efficiency of Flexible Organic Solar Cells via a "Welding" Flexible Transparent Electrode. *Adv. Mater.* **2020**, *32*, 1908478. https://doi.org/10.1002/adma.201908478.

43. He, W.W.; Yan, X.H.; Liang, Y.M.; et al. Scalable and Cost-Effective Ag Nanowires Flexible Transparent Electrodes. *RSC Adv.* **2018**, *8*, 12146–12151. https://doi.org/10.1039/c7ra13196h.

44. Kim, M.G.; Kanatzidis, M.G.; Facchetti, A.; et al. Low-Temperature Fabrication of High-Performance Metal Oxide Thin-Film Electronics via Combustion Processing. *Nat. Mater.* **2011**, *10*, 382–388. https://doi.org/10.1038/nmat3011.

45. Lee, S.H.; Hong, S.; Kim, H.J. Selection of a Suitable Solvent Additive for 2-Methoxyethanol-Based Antisolvent-Free Perovskite Film Fabrication. *ACS Appl. Mater. Interfaces* **2022**, *14*, 39132–39140.

https://doi.org/10.1021/acsami.2c10171.

46. Park, S.; Kim, K.; Jo, J.; et al. In-Depth Studies on Rapid Photochemical Activation of Various Sol–Gel Metal Oxide Films for Flexible Transparent Electronics. *Adv. Funct. Mater.* **2015**, *25*, 2807–2815. https://doi.org/10.1002/adfm.201500545.

47. Kim, H.J.; Jung, J.; Kim, H.J. Enhancement of Electrical Characteristics and Stability of Self-Patterned In–Zn–O Thin-Film Transistors Based on Photosensitive Precursors. *Sci. Rep.* **2020**, *10*, 18853. https://doi.org/10.1038/s41598-020-76080-8.

48. Baltrusaitis, J.; Jayaweera, P.M.; Grassian, V.H. XPS Study of Nitrogen Dioxide Adsorption on Metal Oxide Particle Surfaces under Different Environmental Conditions. *Phys. Chem. Chem. Phys.* **2009**, *11*, 8295–8305. https://doi.org/10.1039/b907584d.

49. Anand, A.; Islam, M.M.; Meitzner, R.; et al. Introduction of a Novel Figure of Merit for the Assessment of Transparent Conductive Electrodes in Photovoltaics: Exact and Approximate Form. *Adv. Energy Mater.* **2021**, *11*, 2100875. https://doi.org/10.1002/aenm.202100875.

50. De, S.; King, P.J.; Lyons, P.E.; et al. Size Effects and the Problem with Percolation in Nanostructured Transparent Conductors. *ACS Nano* **2010**, *4*, 7064–7072. https://doi.org/10.1021/nn1025803.

51. Dressel George, M.G. *Electrodynamics of Solids*; Cambridge University Press: Cambridge, 2002; ISBN 9780511606168.

52. Optical Filters. USA LCC Optical Filters. Available online: https://www.opticalfiltersusa.com/ (accessed on 1 June 2023).

53. Gower, J.C. Generalized Procrustes Analysis. *Psychometrika* **1975**, *40*, 33–51. https://doi.org/10.1007/BF02291478.

54. Bhandari, B.; Bonner, J.C.; Piper, R.T.; et al. Effects of Transparent Conducting Electrodes and Hole Transport Layers on the Performance of MAPbI 3 Solar Cells Fabricated on PET Substrates. *Flex. Print. Electron.* **2024**, *9*, 035002. https://doi.org/10.1088/2058-8585/ad5d01.

55. Kim, S.Y.; Cho, S.J.; Byeon, S.E.; et al. Self-Assembled Monolayers as Interface Engineering Nanomaterials in Perovskite Solar Cells. *Adv. Energy Mater.* **2020**, *10*, 2002606. https://doi.org/10.1002/aenm.202002606.

56. Ali, F.; Roldán-Carmona, C.; Sohail, M.; et al. Applications of Self-Assembled Monolayers for Perovskite Solar Cells Interface Engineering to Address Efficiency and Stability. *Adv. Energy Mater.* **2020**, *10*, 2002989. https://doi.org/10.1002/aenm.202002989.